



## Open Archive Toulouse Archive Ouverte






OATAO is an open access repository that collects the work of Toulouse researchers and makes it freely available over the web where possible

This is an author's version published in: <https://oatao.univ-toulouse.fr/26598>

### Official URL:

<https://doi.org/10.1007/s10596-020-09991-0>

### To cite this version:

Franc, Jacques  and Guibert, Romain  and Horgue, Pierre  and Debenest, Gérald  and Plouraboué, Franck  *Image-based effective medium approximation for fast permeability evaluation of porous media core samples.* (2021) Computational Geosciences, 25. 105-117. ISSN 1420-0597 .

Any correspondence concerning this service should be sent to the repository administrator: [tech-oatao@listes-diff.inp-toulouse.fr](mailto:tech-oatao@listes-diff.inp-toulouse.fr)

# Image-based effective medium approximation for fast permeability evaluation of porous media core samples

Jacques Franc<sup>1</sup> · Romain Guibert<sup>1</sup>  · Pierre Horgue<sup>1</sup> · Gérald Debenest<sup>1</sup> · Franck Plouraboué<sup>1</sup>

## Abstract

An image-based effective medium approximation (EMA) is developed so as to permit very fast transport properties evaluations of 3D porous media. From an image-based porous network (IBPN) built upon digital image processing of 3D binary images, we focus on throat's local geometrical properties at the pore scale, for being the most sensible structural units which build up the local pressure. This approach is a 3D image-based extension of the critical point approach proposed in 2D fractures. We show, from analyzing various core rock samples available in the literature, that the asymptotic assumptions associated with the preeminence of critical points in throats are indeed geometrically relevant. We then describe how the image-based EMA evaluated from the conductances computed from the discrete IBPN can be reliably evaluated. The proposed method is evaluated upon the estimation of core sample permeability from binarized image obtained using X-ray tomography. Since it combines digital image treatments with statistical data post-processing without the need of computational fluid dynamics (CFD) computation, it is extremely cost efficient. The results are compared with a micro-scale Stokes flow computation in various rock samples. The sensitivity to the pore discretization also is discussed and illustrated.

**Keywords** Porous media · Effective properties · Image-based method · Effective medium approximation · Permeability

## 1 Introduction

Image-based pore-scale modeling has progressed significantly during the past decades, due to improvements in X-ray imaging sources and equipments, in image analysis processing, and computational fluid dynamics (CFD) efficiency.

In the following, CFD methods refer to 3D discretization of Navier-Stokes equations up to pore scale. This also obviously includes all Stokes solvers (being the relevant low Reynolds limit of Navier-stokes ones) with any discrete formulation (e.g., finite volumes, finite elements, finite differences, immersed boundaries methods, and lattice Boltzmann method) defined either on structured or unstructured meshes. Obviously pore network models (PNM) do not pertain to CFD methods, since their definition and applications are much narrow.

Nevertheless, the reliability of digital rock physics (DRP) predictions compared with real experiment measurements remains a challenging issue which needs to consider crucially important parameters such as typical pore-scale size, image spatial resolution and quality, representative elementary volume (REV) size compared with sample size, and influence of boundary conditions (see for example [3, 4, 14, 21, 23, 45, 50]). Hence, even if the idea of numerically predicting the transport properties of core samples from 3D images is an attractive long-standing idea in porous media, it faces serious technical difficulties when taking into account all the necessary constraints for reliability. Along the years, these constraints have constantly been impaired by the improvement of image spatial resolution and the

✉ Romain Guibert  
romain.guibert@imft.fr

Jacques Franc  
jfranc@stanford.edu

Pierre Horgue  
pierre.horgue@imft.fr

Gérald Debenest  
gerald.debenest@imft.fr

Franck Plouraboué  
franck.plouraboue@imft.fr

Institut de Mécanique des Fluides de Toulouse, IMFT,  
Université de Toulouse, CNRS, Toulouse, France

parallelization of CFD codes. More recently, deep learning techniques have been applied to permeability determination of 2D and 3D image samples (see [5, 53]).

Nevertheless, this is at the prize with raising efforts associated with numerical cost and efficiency, data, and memory volumes. These limitations for providing reliable estimation of permeability for a given rock sample, from image-based numerical predictions, are well known among the community [44]. In this contribution, we propose a very fast, image-based, and CFD-free method, for the estimation of core sample permeability. The method is based upon combining image processing for building image-based porous network (IBPN) with an adapted effective medium approximation (EMA) [17, 28, 51, 52]. Since the proposed method does not use CFD, it cannot provide a very precise estimate of the permeability. Nevertheless, given the error associated with pore voxelization, any other computational approach will have the same limitation. Furthermore, since, in many cases—rough estimate (e.g., 20%) of the permeability will give a satisfactory answer for many applications—we dedicate our efforts to develop a very efficient, easy to use method without considering accuracy as a major issue.

IBPN have been developed for pore-scale analysis of core samples using various methods and purposes (cf. [18] for a recent review). The IBPN may be constructed from digital image processing using various approaches, without a clearly prevailing one at the present time. One of the most popular methods is the medial axis extraction, generally evaluated with a homotopic thinning [37, 40]. Some further developments of medial axis extraction adding subsequent steps associated with distance map and voxels clustering have also been proposed [27]. Alternative methods using watershed seeded from pore centers have also been tested [46]. Whatever the method considered, IBPN is resource consuming since the closer we get to the percolation threshold, the finer the mesh is needed at constrictions [33]. However, image processing has grown in popularity during the last decade and major progresses have been made with a particular care for implementing efficient algorithms since data volume has proportionally increased with the computer storage capacity and CPU/GPU efficiency. As the binarized tomography images produced from tomography are a usual starting point of 3D object's construction for meshing and simulation, it is also consistent to keep on with digital image processing tools to derive skeleton or to evaluate pore throats diameters. In this paper, we endeavor a new strategy based upon the identification of critical saddle points associated with conductances inside throats connecting two successive pores. Under the assumption of creeping flow, we develop and extent to 3D porous samples the critical point EMA previously proposed in fracture flows [38, 39, 54]. The main idea for evaluating the permeability

of a given core sample is to foresee that constrictions in throats connecting successive pores are the more sensible units for building the pressure drop. The method presented here uses an open-source image processing tool (CImg library [56]) combined with EMA to compute geometric object and physical quantities and hence is named image-based EMA. Such flow approximation can be made in various systems, such as microfluidic system [2], rough fracture, and geophysical rock experiment [6, 22, 35] but also in micro-vascular circulation. The local aperture field is assumed to verify the lubrication theory requirement. Pressure gradients are then flow-determinant in the vicinity of the local saddle point of the aperture field.

This paper is organized as follows. In Section 2, all methodological steps are detailed and the IBPN is discussed. In Section 2.1.1, we describe how critical saddle points in throats can be extracted. In Section 2.1.2, we show how a reliable local conductances evaluation can be tailored. Finally in Section 2.2, we detail how these local conductances can be used within an EMA for providing transport parameters. Section 3 is devoted to the results obtained over a wide range of rocks, previously published in the literature and compared with available results. EMA model and saddle point filtering are highlighted.

## 2 Materials and methods

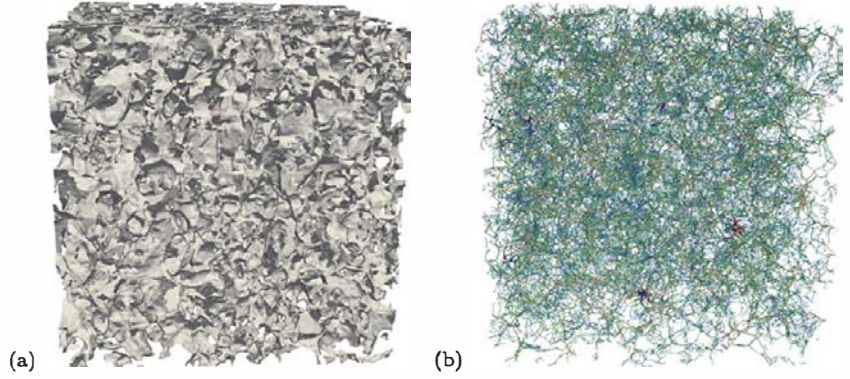
### 2.1 Image-based porous network construction

The binarized void part of the sample produced from thresholding the initial gray-level image is the natural starting point for building IBPN. This construction can be performed using two families of methods [58]. The first family relies on topological properties and dedicated tools [30, 31]. The second family is based upon morphological oriented approaches [7, 8, 29, 59]. Here, we adopt the topological family of methods, in order to elaborate the required IBPN from the binary image's skeleton. There has been extensive efforts to conceive efficient algorithms for skeletonization and we refer the interested reader to [43] for a review. The image processing algorithms are usually discussed within three main groups:

1. Point geometry approaches based upon Voronoï tessellation to construct discrete skeleton using its symmetry properties [47],
2. Surface geometry approaches based upon the continuous evolution of object boundaries [48],
3. Volumetric approaches based upon digital morphological erosion on a distance transform results [10, 13].

In the following, we consider the second family of method, using the Torsello [55] corrected version of Hamilton-Jacobi

Fig. 1 a Smoothed surface representation of Doddington's sample solid part from [41] and b its corresponding Torsello skeleton colored by local radius value obtained



skeleton [16, 48] as implemented in CImg plugin [56] (see Fig. 1 for illustration). The skeleton will be used later as the support for the EMA.

### 2.1.1 Saddle point localization and filtering

The relevance of local saddle points of the aperture map inside throats is based upon the geometrical constraint that the local aperture  $h(x)$  at saddle points is small compared with the distance  $L$  between two connected pores, i.e.,

$$\epsilon = \frac{h(x)}{L} \ll 1. \quad (1)$$

This geometrical asymptotic constriction parameter  $\epsilon$  is illustrated on Fig. 2a. Using real rock core samples taken from [41], we provide in Fig. 2b the probability density function (PDF) distribution of the geometrical asymptotic constriction parameter  $\epsilon$ . The asymptotic constraint  $\epsilon \ll 1$  is fulfilled by each of four different rock types. The Estailades sandstones conspicuously display the most constricted throat, while the Ketton sandstones have the less constricted ones.

Before considering the possible relevance of these geometrical constraints, one first needs to identify the location of the

saddle points inside throats. Vectorized skeleton's edges are progressively traveled in order to localize the locus of minimum aperture in the throats. The curvilinear value of the distance map field along the skeleton is spline-interpolated with respect to the curvilinear distance from start to end along each vectorized edge. Next, first and second derivatives evaluation along the edge provides a list of local minima. In most cases, several local minima are found and tagged as *candidates*. They can be filtered from using one of the three following options:

- (i) No filtering: all minima remains in the set.
- (ii) Lowest filtering: only the lowest local distance transform value per edges is kept.
- (iii) Cluster filtering: the distance transform values are combined based on distance criteria.

Figure 3 illustrates these three filtering options on a selected edge of the network. These filtering choices have an impact on the statistical distribution of the radii at the throat  $r_n$ , as well as on the local conductances which possibly influence the permeability estimation. Keeping all the local conductances with option (i) could result in heterogeneous set of local conductances with a strong dependence upon local voxelization defects. The lowest

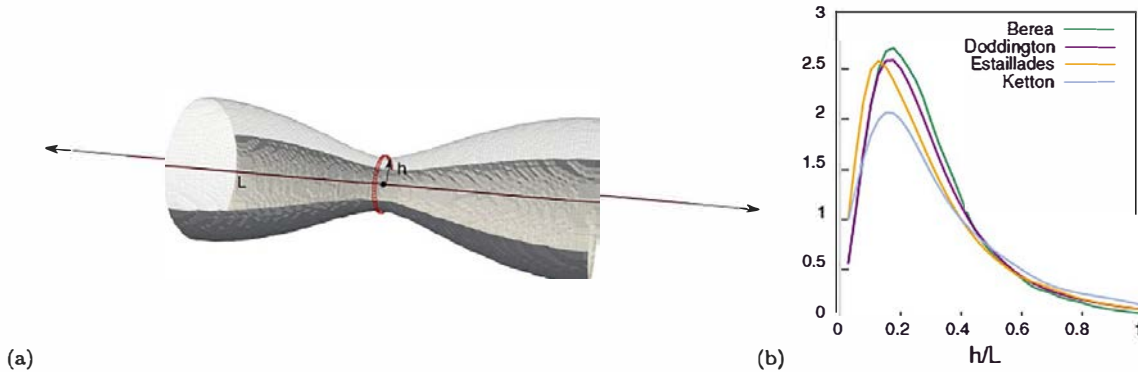


Fig. 2 a Illustration of the asymptotic requirement at the throat location for  $\epsilon = 0.04$ . b Distribution of the geometrical asymptotic constriction parameter  $\epsilon$  for the various samples ( $1000^3$  voxels images)

presented in [41]: Estailades carbonates (mode for  $\epsilon = 0.075$ ), Ketton limestones (mode for  $\epsilon = 0.125$ ), Doddington sandstone (mode for  $\epsilon = 0.175$ ), Bentheimer sandstone (mode for  $\epsilon = 0.175$ )

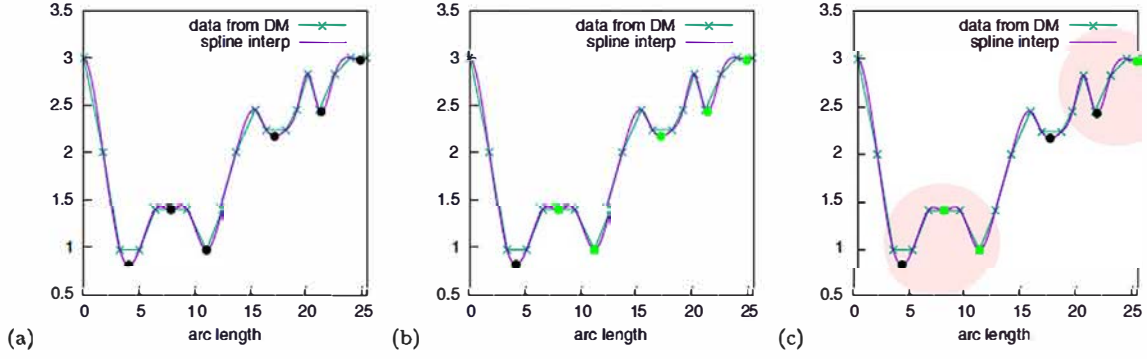


Fig. 3 The local minima filtering methods are illustrated on one of the Bentheimer vectorized skeleton's edge: a no filtering, b lowest kept, and c clustering. Green crosses are voxel values of the distance transform along the selected skeleton edge, purple solid line is its spline

option (ii) under-estimates the local conductance in each edge producing the lower bound for the permeability evaluation. Since the cluster filtering (iii) combines the conductances values, it reduces the distribution variance while concomitantly shortening the sample size used in the statistical pre-processing of the EMA. Finally, having found the saddle points inside throats, one can evaluate locally each parameter  $\epsilon$ .

### 2.1.2 Medialness and finite voxelization corrections

One additional corrective step is required for every saddle-points obtained and filtered. The skeleton quality has indeed not been assessed and building a reliable and robust skeleton in such complex geometries is known as a difficult, method-dependent, and parameter-sensitive issue. The benchmarking of skeletonization algorithms has been partially neglected in past studies and even if it would be necessary to deepen this aspect, it is far beyond the scope of this contribution. It would necessitate ground-truth evaluation obtained in various families of rock types and many other systematic comparisons. Here we adopt, a pragmatic approach, proposing a medialness correction to impair skeletonization default. The medial-line is characterized as the following locus of voxels,

$$M = \{x_k \in P_i \mid \min_{x_k} (\nabla DT(x_k))\}, \quad (2)$$

denoting  $P_i$  as the perpendicular plane to the skeleton's local tangent at the saddle point of position  $x_i$ , and  $DT(x)$  as the distance map transform application.

For each pair  $\{x_i, r_n\}$ , the  $9 \times 9 \times 9$  neighborhood is thresholded for voxels having a lower gradient value  $\nabla DT(x_i)$  (see Fig. 4a). The candidates for medialness correction consist in a set of distinct connected components voxels. The barycentric position  $\{x_{c,j}\}$  can be defined for each connected components candidate (see Fig. 4b). To select the proper location for the medialness correction

interpolation, green circles are local minima, and black highlighted circles are the candidate selected by filtering. On c, pink circles are considered areas for clustering

among the candidates, we consider that it has to be a saddle point value of the distance map transform field. Hence, the proper candidate should both be a local maxima inside plane  $P_i$  and a local minima along the medial axis direction. The selected candidate located in  $x_c^*$  should thus verify the geometrical constraints,

$$x_c^* = \min_{x_{c,j}} |\langle x_i \cdot x_{c,j} \rangle|, \quad (3)$$

in order to constrain it to be the nearest point to the perpendicular plane  $P_i$  (see Fig. 4c). This medialness corrective step maximizes the local radii values of the saddle points, and so it does to the associated local conductances.

The second correction step, i.e., finite-size voxelizations correction, is required because when the number of voxels inside each throat is small (typically smaller than five), the voxelization of the geometry has non-negligible influence on the numerical evaluation of local conductances.

As a matter of fact, any numerical computation is sensitive to voxelization. Image-based geometrical approach consists in finding the best approximation  $r_{0ib}$  of the local radius  $r_0$  using the distance transform map. Obviously, the distance transform directly suffers from voxelization defects leading to an approximate radius  $r_{0ib}$ . Under low Reynolds assumptions in the tube, the local conductance (resulting from a Poiseuille profile)  $g_{ib}$  can be analytically estimated

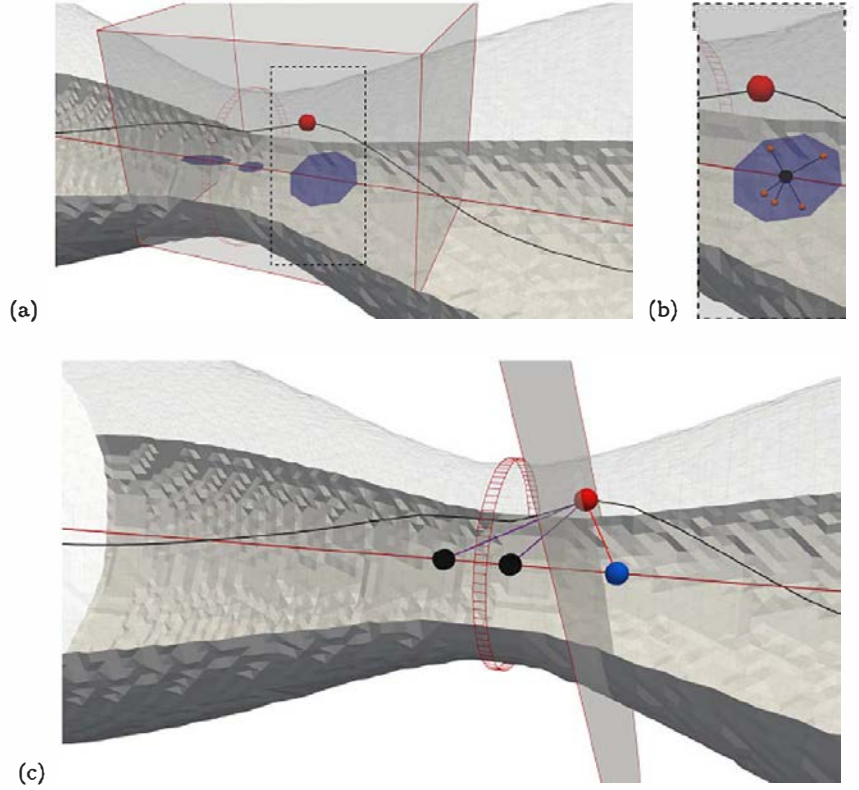
$$g_{ib} = \frac{\pi r_{0ib}^4}{8\mu}. \quad (4)$$

### 2.1.3 Throat conductance evaluation

The local conductance  $g_c$  is the pre-factor which relates the local pressure drop  $\Delta p$  and the fluid flux  $q$  inside each throat

$$q = \frac{g_c}{\mu} \Delta p \quad (5)$$

**Fig. 4** Sketch of the medialness correction geometrical algorithm: a the  $9 \times 9 \times 9$  neighborhood of the selected (red) dot is threshold for area with a lower value of  $\nabla DT(x)$ , b candidates are tagged in orange and their barycenter is found (it results in one point per area), c the medial axis is reported with a red line (a straight line in this simple case) while the black line represents the skeleton. The red dot is the saddle point found along the skeleton, when traveling across. The black and blue points are medialness point correction candidates. They are maxima of distance transform, verifying relation (2). The blue point is finally the one selected as being the closer to the (gray) plane  $P_i$ , locally perpendicular to the skeleton's local tangent at the saddle point location



Using an asymptotic approach similar with the one derived in [39] in two-dimensional configuration, it is possible to show that (cf. Appendix A) the effective conductance of each throat is given by the discrete contribution of conductance in each critical point previously defined (see Section 2.1.1), when  $\epsilon = \sqrt{r_0 r_{zz}} \ll 1$  with  $r_{zz}$  being the second derivative of the throat's radius at the saddle point (which is a fair approximation of the surface curvature, at this point)

$$g_c = \frac{2\sqrt{2} r_0^4}{5 \epsilon}. \quad (6)$$

This result is consistent with the results available in [9].

## 2.2 Image-based EMA method

This image-based EMA method is an extension to 3D sample of the critical point EMA method previously proposed in the context of fracture flows modeling [38, 54]. The critical point approach is based upon the approximation that the main pressure drops happen at most constricted throats which then drive the flow. Hence, a detailed local description at these spots should provide a good estimate of the transport properties. In some sense, this approximation is a first-step upscaling associated with a lubrication to Stokes matching. The EMA is used to approximate a randomly connected conductance network. The EMA is valid when the considered network is far from the

geometrical percolation threshold, i.e., one needs to build a pore-to-throat network whose links connect the input faces to the output faces in most cases. It can be noted that the second constraint is also implicitly adopted when using DNS to evaluate permeability since simulation on non-percolant samples is not possible.

In order to estimate the permeability, the proposed EMA uses local estimation of the conductance using Eq. 4 or Eq. (6) at the pore throats to form new pairs  $\{x_i, g_n\}$ . Introducing the PDF of the conductances  $g_n$  as  $p(g_n)$ , the following integral equation can be solved for the macroscopic conductance  $G_n$  [54]:

$$\int_0^\infty \frac{g_n - G_n}{g_n + ZG_n} p(g_n) dg_n = 0 \quad (7)$$

using the reduced network coordinance  $Z$ , with  $z$  the coordinance, i.e., the number of incident paths inputting and outputting from a pore (respectively network's node),

$$Z = \frac{z}{2} - 1. \quad (8)$$

In order to solve (7), it is required to derive the PDF  $p(g_n)$ . It is done using kernel density estimation (KDE) library [15, 26] with asymptotic mean integrated squared error (AMISE) bandwidth estimator. As the conductances are physically defined to be positive, the kernel is approximated to be Gaussian distributed for the logarithm values of local conductances  $\ln(g_n)$ . The last step is then to solve (7) for  $G_n$ .

The complete image-based EMA algorithm presented in Sections 2.1 and 2.2 is synthesized on Alg. (1) as on Fig. 5.

---

**Algorithm 1** Image-based EMA algorithm step by step.

---

**Require:** Binarized core sample image

- 1: Get the Distance Transform [Euclidian]
  - 2: Get the Skeleton [Torsello corrected Hamilton-Jacobi]
  - 3: Evaluate the reduce coodinance  $Z$  (8) of the Skeleton-network
  - 4: **for** all network edges  $e_i$  **do**
  - 5:     Localize local minima
  - 6:     Correct medialness
  - 7:     Filter obtained values
  - 8:     Evaluate conductances  $\{g_n\}$  from Eqs. 4 or 6
  - 9: **end for**
  - 10: Construct PDF  $p(g_n)$  using KDE [Gaussian kernel with AMISE optimal]
  - 11: Solve the EMA integral (7)
- 

### 2.3 Algorithm complexity

Referring to Fig. 5, the bottleneck step is found during the image processing stage. Local treatments are performed on a restricted set of voxels, the dimension of which is orders of magnitude lower than the whole core sample image. The EMA system solution is computationally cheap for similar reason. Both computational complexity and memory cost are then driven by the implementation choices for the distance map and skeletonization. The distance transform is implemented following the algorithm proposed in [34]. It consists of an approximation of the squared Euclidian distance using sequential directional sweeps after initialization. The computational complexity is  $\mathcal{O}(6n)$  in terms of numbers of operations,  $n$  being the number of voxels of the image. The memory cost is also dominated by  $\mathcal{O}(am)$  for peak-use,  $a$  being the pre-factor depending on the chosen type (i.e., float or double) to store distance information and  $m$  the byte size of the initial binary image. The skeletonization used in this work is based on [16]. It consists in two stages, the first is associated with the discovery of the end points having an  $\mathcal{O}(n)$  complexity, the second being graph traversing/discovering also of  $\mathcal{O}(n)$  complexity. The memory costat peak reaches  $\mathcal{O}((5a + 2)m)$  because of flux correction steps [55] which are required to produce the final skeleton. The above-mentioned computational complexity and memory cost are confirmed by various test runs on subdivisions of a  $128^3$  voxels binary image reported in Table 1 on an Intel (R) Core(TM) i5-10210U CPU @ 1.60GHz with 2 x 4096 MB DDR4 RAM. ib-EMA allows to run up to  $1000^3$

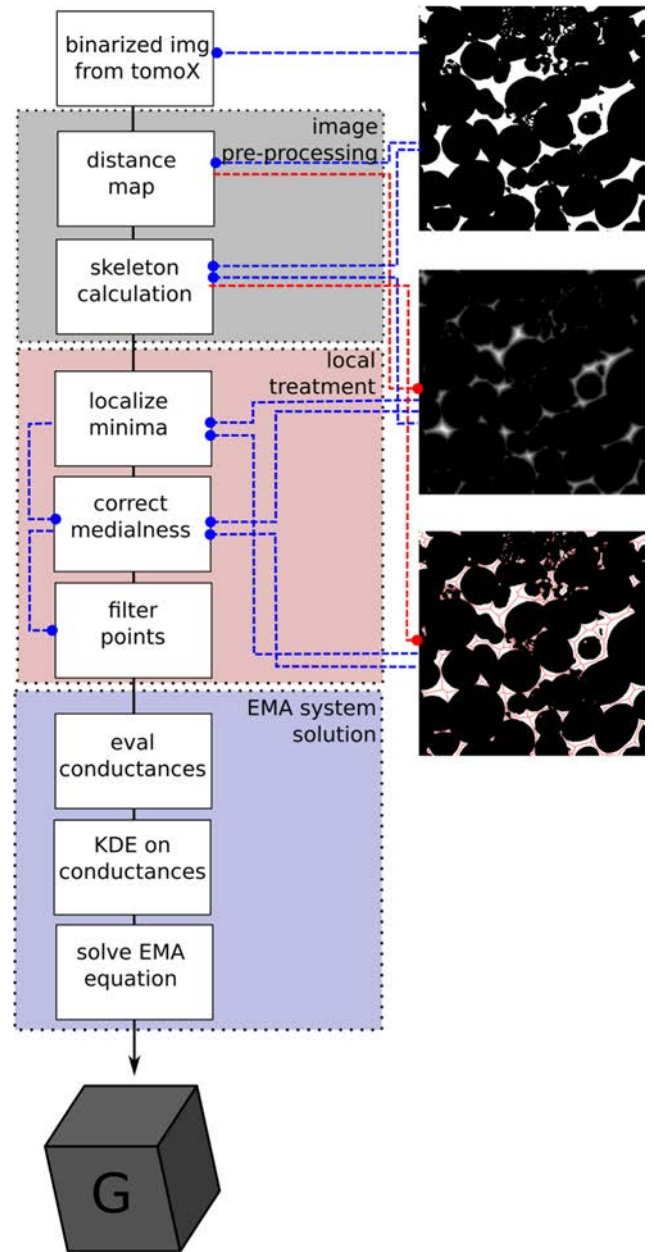


**Fig. 5** Graphical representation of the proposed image-based EMA algorithm for permeability estimation directly from 3D binary images

core sample on a desktop station. Finally it is interesting to mention that efficient parallel implementations for both distance transform [19, 32] and skeletonization [20] are active research topics.

Running the same  $128^3$  voxels image with the CFD OpenFOAM tools [23, 25], the observed memory cost also scales linearly, i.e.,  $\alpha n$ . However since the  $\alpha$  factor is close to 50, it leads to a memory cost of 128Mb for a  $128^3$  voxels image. This memory cost reaches 230Gb for a more realistically sized core image of  $1000^3$  voxels. This impediment running CFD computation for larger

**Table 1** Computational and space complexity of ib-EMA algorithm tested on  $128^3$  core images using gperf tools [49]

Case (size)	Distance map		Skeletonization	
	Peak (Mb)	Runtime (ms)	Peak (Mb)	Runtime (ms)
Eighth (264Kb)	2	370	11	39,060
Quarter (520Kb)	5	670	23	84,160
Half (1.1Mb)	10	1280	46	178,540
Whole (2.1Mb)	20	3980	93	368,310
Order	$\sim o(8m)$	$o(n)$	$\sim o(42m)$	$o(n)$

image samples on a desktop laptop. On the other hand, the computational complexity of CFD computations is limited by two key hindrances: the void space meshing and the Stokes solver. The first one is the subject of ongoing optimization, while the Stokes solver iterates until convergence using a classical implementation of a geometric agglomerated algebraic multigrid. The numerical cost of the implemented method has been tested and it scales linearly with the size of the problem ranging from 2 min on our small  $128^3$  voxels image to a 16-h run on a  $1000^3$  voxels image on a single core.

### 3 Results and discussions

#### 3.1 Validation

To validate the method, we confront it with direct numerical simulations on simple and idealized objects, simply solving Stokes' equation. These simulations are carried out with the open-source finite volume library OpenFOAM [57] which is widely used in the community. Notably, the very same CFD software was also used in the reference study [41] in order to characterize real rocks. Furthermore, OpenFOAM is also used in several recent studies dealing with real porous media [23, 25], and also for other physical configurations such as two-phase flows [42], particle transport [11], inertial flows [36], or compressible flows [24].

##### 3.1.1 Straight tube

The finite-size voxelization correction is illustrated inside a straight cylinder having a diameter  $r_0$  in Fig. 6. Changing the number of voxels (from 1 to 25 per radius) used to discretize the circular edge of the cylinder, we compare the true theoretical conductance with the image-based geometrical approach as well as with a finite volume CFD numerical evaluation (over the structured grid of voxels). These grids are castellated, mimicking the voxelization of original binarized image. The chosen procedure neither introduces bias nor needs additional smoothing parameters for surface generation.

Figure 6 then displays the ratio between the numerically estimated conductances and the analytical value for various degrees of voxelization. It is interesting to observe that the image-based evaluation always under-estimates the conductance. However, for small voxel number inside the cylinder, we hereby provide a simple way to correct the

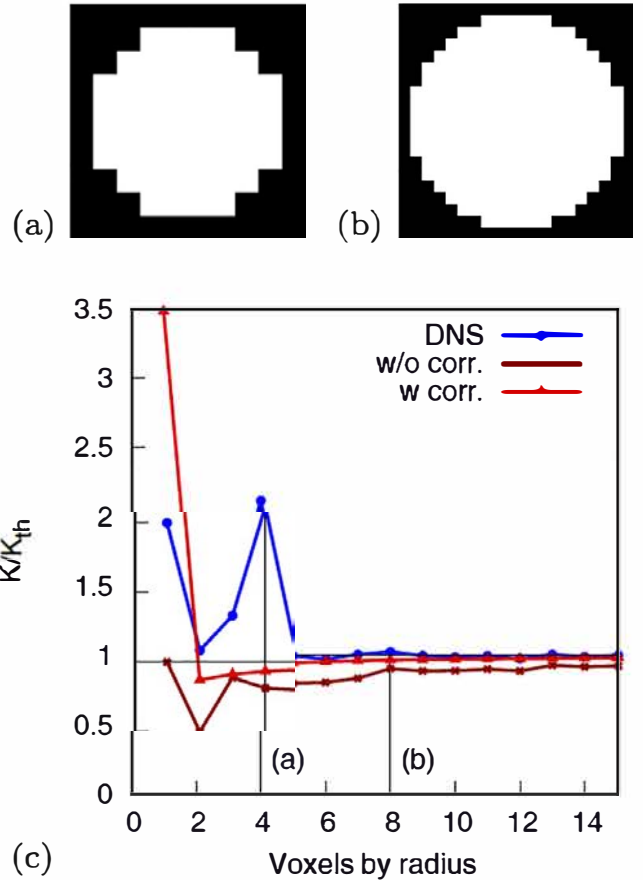


**Fig. 6** Illustration of finite-size voxelization effect on the evaluation of the conductance inside a tube. Example of voxelized tube section for a 4-voxels per radius and b 8-voxels per radius. c compares predicted permeability with those obtained with direct numerical simulations (blue bullets), basic distance map (w/o corr, upper brown star), and the proposed finite-size corrected distance map (w corr, upper red triangle symbols). All estimations are normalized by the expected theoretical result, so that one is the expected asymptotic limit



image-based estimate. Our voxelization correction applies when there are various candidate voxels for being the local maxima of the distance transform map, i.e., various voxels for which the distance map has a maximal value. In the cylindrical case, in the transverse plane, the four central voxels are all possible candidates for the local maxima of the aperture map. Our voxelization correction consists in adding to the value of the distance map inside the candidate voxels, the average distance between each candidate and the barycenter of the candidate's group. From doing so, a small correction can be applied to  $r_{0ib}$ , providing a much better estimate of the local conductance, as shown in Fig. 6.

### 3.1.2 Idealized throat

The surface curvature approximation is compared into an idealized constriction with a CFD approximation for various  $\epsilon$  values. The throat radius is defined by  $r(z) = R_o - \alpha \sin(\frac{2\pi}{\lambda}z)$  over a half-period. This leads to a parabolic variation of small parameter  $\epsilon$  with respect to  $\alpha$  variations with a maximal value for  $\alpha_M = R_o/2$ . The cases where  $\alpha \in ]0, \alpha_M[$  are qualified as “near-tube” cases, whereas when cases with  $\alpha > \alpha_M$  are considered as “constricted” ones. Monitoring the conductances values obtained using direct numerical simulations (DNS) of Stokes' equations will allow us to assess the validity range of Eqs. 4 and 6 as the throat's curvature increases. The conductances values

associated with Eqs. 4 and 6 are reported versus  $\alpha = R_o - r_o$  at the constriction in Fig. 7 and confronted to the values obtained from DNS. These simulations have been run on castellated grids extracted from generated binarized images, so that the smallest radius is always composed of ten voxels (ensuring mesh convergence as shown in Fig. 6c). They validate (6) in the white zone (i.e., for  $\alpha > 8$ ) since it asymptotes the theoretical curve (in red in Fig. 7) as the throat gets more and more constricted. The  $L_2$  relative error between the developed model and DNS values versus small parameter  $\epsilon$  is also reported in Fig. 7d. The model is taken to be (4) for near-tubes cases and Eq. 6 for more constricted ones, following the best choice illustrated in Fig. 7c.

### 3.2 Method's parametrization

Like most image-based methods, the hereby proposed one requires parameters that are calibrated from the observations and analysis of the results, depending on the original image quality and resolution. This is the case for the flux threshold in the skeletonization step where several values have been tested to finally define the value of the threshold limiting the appearance of spurious branches. The same applies to neighborhood box size of the medialness geometrical correction step which must be enough large to capture the possible neighboring points without varying the initial box size. Note that the tests carried out permit to converge

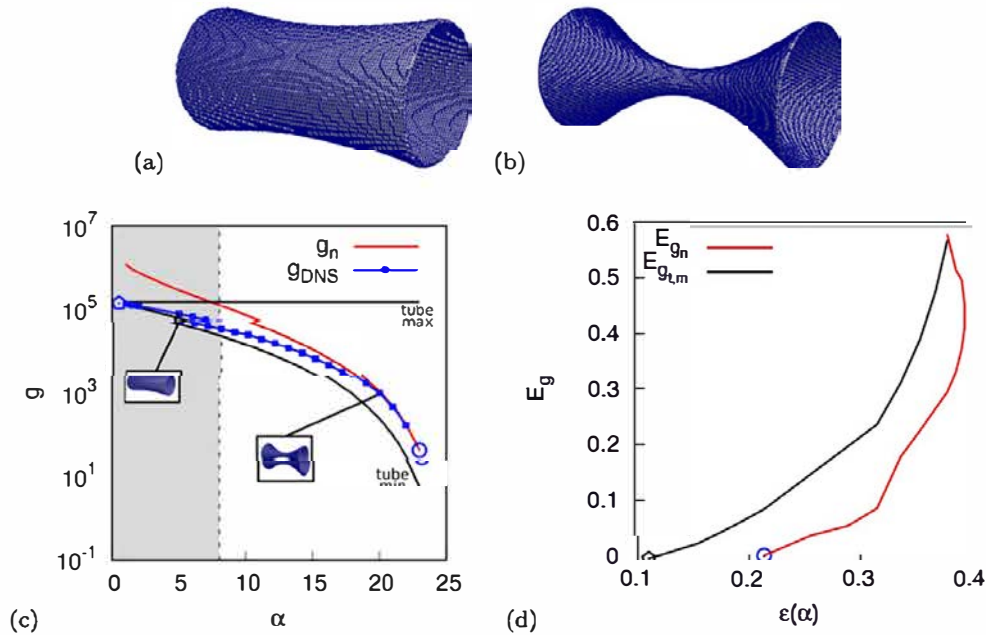


Fig. 7 Illustration of curvature corrected formula on an ideal throat. a and b exemplify two generated throats. a  $(R_o, \alpha) = (25, 5)$  and b  $(R_o, \alpha) = (25, 20)$ . c Variation of conductance values with respect to  $\alpha$  parameter either computed by curvature corrected formula (6) in red or (4) for maximal tube or minimal tube (resp. horizontal and decreasing black lines). d DNS relative error to a reference conductance versus

small parameter  $\epsilon$ . The reference conductance is taken as in Eq. 6 for the minimal tube or radius  $r_o$  for  $\alpha < 8$  (gray area on c) and as in Eq. 6 for  $\alpha > 8$  (white area on c). The blue circle at the end of ( $\alpha > 8$ ) branch exhibits an error increase in DNS values due to a poor discretization at the throat

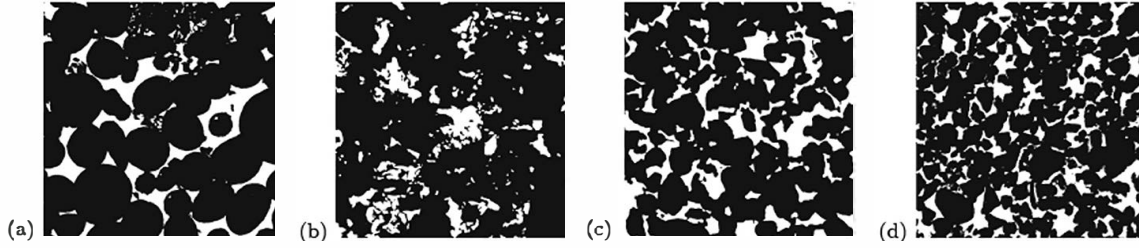


Fig. 8 Rock facies of core samples from [41], respectively, a Ketton and b Estaillasses limestones and c Doddington and d Bentheimer sandstones

towards an optimal box size which is dependent on the image resolution at the throat

In addition, some heuristic choices have been made for the different methods and algorithms used but others would also be justifiable and operable without changing the principle of the EMA developed herein. This is notably the case for the spline interpolation method used for radius evaluation. Since permeability is highly dependent on conductance evaluation (and thus on radius), we found appropriate to use a high order method rather than a simpler linear or cubic method. Similarly, the KDE associated with the AMISE bandwidth estimator allowed us to obtain easily integral distributions but alternatives could possibly be just as effective.

### 3.3 Permeability estimation on real porous media samples

The main interest of the proposed method is to provide a fast and reasonable estimate of permeability directly from the 3D images, without using CFD, e.g., finite volumes or lattice Boltzmann methods. Thus, a set of images representative of the various rocks encountered in DRP has been chosen for testing the proposed method. As a preamble to this section, we can observe on Fig. 2b that the parameter  $\epsilon$  is sufficiently small for the considered rock samples (mode is about 0.2). This confirms the relevance of the considered asymptotic approximation, a prerequisite of our image-based EMA. The core samples considered for the image-based EMA validation have been introduced in Secion 2. A selected slice of each of them is presented in Fig. 8. These data have been used in several studies [1, 11, 12, 41], as mentioned in [41]. The images have been

classically obtained using micro-computed tomography and binarized using a watershed segmentation algorithm. For each image, formed of  $1000^3$  voxels, the resolution is reported in Table 2 along with the numerical reference values for porosity and permeability. We have cross-validated the DNS permeability evaluations provided in [41] and obtain very similar results.

The relative error of the proposed image-based method to the reference DNS values [41] is presented in Table 3 depending on the three parametrization methods: the cylindrical (4) conductance with lowest filtering, the cylindrical (4) conductance with cluster filtering, or the curvature corrected (6) conductance with lowest filtering. Note that the use of clustering-based filtering in the case of curvature approximation is not tested since it does not represent a consistent choice. As a matter of fact, clustering-based filtering is based upon the proximity of the throat center without considering individual curvature. As for the CFD permeability evaluation, the EMA method is used considering the largest connected component of the void space in the binarized images. However, one has to keep in mind that the image-based EMA method does not require to remove non-percolating components contrary to CFD evaluations. However, for the considered images, the non-percolating components represent a small percentage of the total empty space and does not significantly modify the conductance statistics.

CFD computations display finite-size sensitivity, whose origin is discussed in Section 3.1.1. As stressed in [23, 25] even if CFD provides a sensible approximation of the permeability, it is difficult to assess its precise accuracy even when the discretization condition of a minimum of five voxels per constriction is fulfilled. It might turn that,

Table 2 Global information on core samples used to evaluated the method

	Ketton	Estaillasses	Doddington	Bentheimer
Resolution ( $\mu\text{m}$ )	3.00	3.311	2.693	3.003
Porosity (—)	0.132	0.109	0.194	0.216
Permeability ( $10^{-12} \text{ m}^2$ )	5.91	0.218	3.76	3.55

These data are provided in [41]. The original binarized images have a size of  $1000^3$  voxels. The permeability evaluations are obtained using CFD for a spatial discretization equivalent to the image voxels one

**Table 3** Relative error of the proposed image-based EMA method to DNS results provided in [41] for permeability estimations

	Ketton	Estailades	Doddington	Bentheimer
Cylindrical approx. + Filter lowest	38%	100%+	63%	57%
Cylindrical approx. + Filter cluster	28%	100%+	51%	44%
Curvature approx. + Filter lowest	6%	100%+	20%	21%

refining the mesh below the image resolution, result in a noticeable influence on permeability evaluations.

Hence, using the most favorable parametrization (last line of Table 3) provides for three typical samples (Ketton, Doddington, and Bentheimer) a value of permeability close to 10 to 20% of the value given using CFD. Furthermore, whatever the chosen parametrization, the EMA method provides poor predictions for one sample (Estailades). This result was expected since this sample is very close to the percolation threshold, a specific case for which EMA method fails. This type of rock is a carbonate, well known for their very strong heterogeneities, closer to a disordered fracture/matrix model than a pore/throat network. On the contrary, Ketton sample is similar to the compaction of nearly spherical objects. In this case, one can observe that the estimation is clearly improved using curvature corrected approximation.

Now discussing the variant of the EMA method, provided in Table 3, it should be noted that clustering the saddle point conductances has a beneficial effect when considering the tube-like (4) conductance model. Since there is no geometrical correction for taking into account the local curvature of the throat with this model, the combination of tube-like approximations in series for the various minima of a throat provides an improvement compared with only considering the lowest constriction. On the other hand, the use of curvature correction for single constriction consideration improves the estimation for each case and even more in the Ketton case.

Hence, for porous media sufficiently far from percolation threshold, we found that the proposed image-based CFD-free method provides a satisfactory approximation of the permeability. These results also confirm the relevance of a “critical-point” approach to pore-scale modeling. Indeed, we found that the small parameter  $\epsilon$  related to the principal curvature ratio at the throat’s saddle points is always small enough so as to justify the use of lubrication approximation inside the throat. To our knowledge, this important geometrical issue has not been reported previously from real images in core samples. We believe that other pore-scale modeling problems might benefit from this asymptotic framework.

From the construction of the methods arises the definition of a statistical representative sample similarly to a representative elementary volume. Reaching this limit is attempted in sub-sampling core images. Indeed, as long as the sub-sampling provides enough data, while not drastically changing the pore-size distribution, the algorithm should then still give accurate results. This is tested on the previously presented type of rocks. The results are summarized on Fig. 9. The whole set of core images are then divided into 8 equal sub-blocks and the throat data are extracted from them. The numerical processing of ib-EMA is then run onto each sub-block and compared with the original estimation. The resulting statistics are then reported in Fig. 9. Despite the cuts, the Doddington and Bentheimer rocks keep a robust distribution of conductance. They then lead to the smallest variation from the entire sample. The sub-sampling is satisfying the elementary representativity constraint. On the other hand, the Ketton rock, which is composed of large interconnected pores, is providing highly variable and deteriorated results after sub-sampling. The



**Fig. 9** Subsampling tests from Cartesian grid partitioning of the  $1000^3$  voxel images. A boxplot representation of the permeability estimation is sketched for the four samples previously considered in Table 3. The ratio between each sub-sample permeability estimation to the reference image permeability estimation is represented so as to illustrate the statistical fluctuations resulting from downscaling the reference volume

Estailades rock, which is close to the limiting case of non-percolating rocks, is also leading to up to 30% variation on the estimates by cutting.

Finally it is interesting to mention that the limitation of the proposed method regarding geometrical and statistical properties of the core sample shares many similar features with other DRP methods. Indeed, in these methods, a reliable permeability estimation necessitates the sample size being larger than REV. In the presented method, we also need the number of pores to be large enough for being robust to finite sampling effects, but this constraint also holds for any DRP approach.

However, the proposed method makes it possible to evaluate the sensitivity to REV without additional calculation, only in post-processing, and without boundary condition effects. Finally, a more specific limit of the presented method is related to the closeness to percolation threshold. Since EMA is known to provide poor results near percolation, our image-based application of EMA also shares this limit. Nevertheless, such limitation is not absolutely diriment for applicative relevance of the method since most core samples share porosity around 20% and most often display largely interconnected structures.

## 4 Conclusion

In this work, a new image-based pore network method based upon the identification of saddle points inside throats coupled with lubrication analysis of the flow has been developed. It is largely inspired by previous work on 2D fractures but its adaptation to 3D core samples has required specific image processing steps as well as adapted asymptotic considerations. The proposed approach is validated on simple and idealized objects, and then compared with the usual CFD method used in the porous media community for the estimation of permeability on real objects of large sizes. The obtained results are satisfactory compared with CFD ones. In addition, this approach has a distinct potential advantage in terms of computational time. This efficiency has even room for improvement if the most detrimental step, e.g., skeletonization could be parallelized, a task which might necessitate further developments. In the future, it is also conceivable to couple the proposed approach with a “thumbnail” imaging method, as long as some statistical convergence criteria are met.

**Acknowledgments** We acknowledge PERM Group at Imperial College London to publicly share their binarized image sets.

**Funding information** This study was financially supported by Carnot Institute ISIfOR with ESTIME project. This work was performed using HPC resources from CALMIP (Grant P13147).

## Compliance with ethical standards

**Conflict of interest** The authors declare that they have no conflict of interest.

## Appendix

### A conductance of an axisymmetrical tubular throat

In this section, we show how the leading order approximation for the conductance inside a tubular throat is given by Eq. (6). We consider Stokes equation associated with the velocity field  $\mathbf{u}$ , the pressure  $p$ , and the dynamic viscosity  $\mu$

$$\mu \Delta \mathbf{u} - \nabla p = 0, \quad (9)$$

inside an axisymmetrical tubular throat having a variable radius  $R(z)$  along the longitudinal direction  $z$ , considering cylindrical coordinates  $(r, \theta, z)$  (as the one represented in Fig. 2a). We chose the origin of the coordinate system at the throat minimum radius  $r_0$ , so that  $R(z = 0) = r_0$ . We consider a finite length throat where a fixed pressure drop is applied at edges  $z = \pm L/2$ . Using the usual lubrication non-dimensionalization  $\mathbf{u} = U(\epsilon u_r, \epsilon u_\theta, u_z)$ , where  $U$  is the main longitudinal velocity along the  $z$  direction. From axisymmetry  $u_\theta = 0$ . In the vicinity of the constriction, the following Taylor expansion of the local radius is

$$R(z) = r_0 \left( 1 + \frac{1}{2} \frac{R_{zz}}{r_0} z^2 + \dots \right).$$

Considering tilde dimensionless variables,  $r = \tilde{r} r_0$ ,  $R = \tilde{R} r_0$  and  $z = \tilde{z} \frac{r_0}{\sqrt{r_0 R_{zz}}}$ , one finds

$$\tilde{R}(\tilde{z}) = \left( 1 + \frac{1}{2} \tilde{z}^2 + \dots \right).$$

Using  $\epsilon = \sqrt{r_0 R_{zz}} \ll 1$  as a small parameter, one can seek for an asymptotic expansion the velocity and pressure

$$\tilde{u}_{\tilde{r}} = \tilde{u}_{\tilde{r}}^0 + \epsilon \tilde{u}_{\tilde{r}}^1 + ..$$

$$\tilde{p} = \tilde{p}^0 + \epsilon \tilde{p}^1 + ..$$

when inserted into the expansion in power of  $\epsilon$  of the operators of the Stokes problem (9) leads to the following leading order problem

$$\frac{1}{r_0 \tilde{r}} \frac{\partial}{\partial \tilde{r}} \left( \tilde{r} \frac{\partial \tilde{u}^0}{\partial \tilde{r}} \right) - \frac{\epsilon}{r_0} \frac{\partial \tilde{p}^0}{\partial \tilde{z}} = 0.$$

The solution of this problem can be found easily

$$\tilde{u}^0 = \frac{\epsilon}{4} \frac{\partial \tilde{p}^0}{\partial \tilde{z}} (\tilde{r}^2 - \tilde{R}^2).$$

Computing the resulting leading order flux  $\tilde{q}^0$  from integrating the velocity in cylindrical coordinates between 0 and  $\tilde{R}(\tilde{z})$  leads to

$$\tilde{q}^0 = -\frac{\pi\epsilon}{8} \frac{\partial \tilde{p}^0}{\partial \tilde{z}} \tilde{R}^4.$$

Looking for the head pressure loss gradient  $\partial_{\tilde{z}} \tilde{p}^0$ ,

$$\frac{\partial \tilde{p}^0}{\partial \tilde{z}} = -\frac{8\tilde{q}^0}{\pi\epsilon} \tilde{R}^{-4},$$

integrating between 0 and  $\tilde{z}$ , considering  $\tilde{p}(0) = 0$  as pressure reference,

$$\tilde{p}^0(\tilde{z}) = \left[ \frac{5}{16} \sqrt{2} \arctan\left(\frac{\tilde{z}}{\sqrt{2}}\right) + \frac{15\tilde{z}^5 + 80\tilde{z}^3 + 132\tilde{z}}{24(\tilde{z}^2 + 2)^3} \right] \left( -\frac{8\tilde{q}^0}{\pi\epsilon} \right),$$

and considering limits for an infinitely long throat,

$$\lim_{\tilde{z} \rightarrow +\infty} \tilde{p}^0 = \frac{5\epsilon}{\sqrt{2}} \tilde{q}^0,$$

finally provides the following conductance for the whole throat:

$$G_n = \frac{2\sqrt{2}}{5} \frac{r^4}{\epsilon}.$$

## References

- Alhashmi, Z., Blunt, M., Bijeljic, B.: The impact of pore structure heterogeneity, transport, and reaction conditions on fluid–fluid reaction rate studied on images of pore space. *Transp. Porous Media* **115**(2), 215–237 (2016)
- Amyot, O., Plouraboué, F.: Capillary pinching in a pinched microchannel. *Phys. Fluids* **19**(3), 033101 (2007)
- Andrae, H., Combaret, N., Dvorkin, J., Glatt, E., Han, J., Kabel, M., Keehm, Y., Krzikalla, F., Lee, M., Madonna, C., Marsh, M., Mukerji, T., Saenger, E.H., Sain, R., Saxena, N., Ricker, S., Wiegmann, A., Zhan, X.: Digital rock physics benchmarks-part I: imaging and segmentation. *Comput. Geosci.* **50**, 25–32 (2013)
- Andrae, H., Combaret, N., Dvorkin, J., Glatt, E., Han, J., Kabel, M., Keehm, Y., Krzikalla, F., Lee, M., Madonna, C., Marsh, M., Mukerji, T., Saenger, E.H., Sain, R., Saxena, N., Ricker, S., Wiegmann, A., Zhan, X.: Digital rock physics benchmarks-part II: computing effective properties. *Comput. Geosci.* **50**, 33–43 (2013)
- Araya-Polo, M., Alpak, F.O., Hunter, S., Hofmann, R., Saxena, N.: Deep learning–driven permeability estimation from 2D images. *Comput. Geosci.* 1–10 (2019)
- Auradou, H.: Influence of wall roughness on the geometrical, mechanical and transport properties of single fractures. *J. Phys. D: Appl. Phys.* **42**(21), 214015 (2009)
- Bakke, S., ØRen, P.E., others: 3-D pore-scale modelling of sandstones and flow simulations in the pore networks. *SPE J.* **2**(02), 136–149 (1997)
- Baldwin, C.A., Sederman, A.J., Mantle, M.D., Alexander, P., Gladden, L.F.: Determination and characterization of the structure of a pore space from 3D volume images. *J. Colloid Interface Sci.* **181**(1), 79–92 (1996)
- Bernabé, Y., Olson, J.F.: The hydraulic conductance of a capillary with a sinusoidally varying cross-section. *Geophys. Res. Lett.* **27**(2), 245–248 (2000)
- Bertrand, G.: On p-simple points. *Comptes Rendus de l'académie des Sciences. Série Math.* **1**(321), 1077–1084 (1995)
- Bijeljic, B., Mostaghimi, P., Blunt, M.J.: Insights into non-fickian solute transport in carbonates. *Water Resour. Res.* **49**(5), 2714–2728 (2013)
- Bijeljic, B., Raeini, A., Mostaghimi, P., Blunt, M.J.: Predictions of non-Fickian solute transport in different classes of porous media using direct simulation on pore-scale images. *Phys. Rev. E* **87**(1), 013011 (2013)
- Blum, H.: Biological shape and visual science (part I). *J. Theor. Biol.* **38**(2), 205–287 (1973)
- Blunt, M.J., Bijeljic, B., Dong, H., Gharbi, O., Iglauer, S., Mostaghimi, P., Paluszny, A., Pentland, C.: Pore-scale imaging and modelling. *Adv. Water Resour.* **51**, 197–216 (2013)
- Botev, Z.I., Grotowski, J.F., Kroese, D.P., et al.: Kernel density estimation via diffusion. *Ann. Stat.* **38**(5), 2916–2957 (2010)
- Bouix, S., Siddiqi, K., Tannenbaum, A.: Flux driven automatic centerline extraction. *Med. Image Anal.* **9**(3), 209–221 (2005)
- Bruggeman, V.D.: Berechnung verschiedener physikalischer konstanten von heterogenen substanzen. i. dielektrizitätskonstanten und leitfähigkeiten der mischkörper aus isotropen substanzen. *Ann. Phys.* **416**(7), 636–664 (1935)
- Bultreys, T., De Boever, W., Cnudde, V.: Imaging and image-based fluid transport modeling at the pore scale in geological materials: a practical introduction to the current state-of-the-art. *Earth-Sci. Rev.* **155**, 93–128 (2016)
- Cao, T.T., Tang, K., Mohamed, A., Tan, T.S.: Parallel banding algorithm to compute exact distance transform with the GPU. In: *Proceedings of the 2010 ACM SIGGRAPH symposium on Interactive 3D Graphics and Games*, pp. 83–90 (2010)
- Deng, W., Iyengar, S.S., Brener, N.E.: A fast parallel thinning algorithm for the binary image skeletonization. *Int. J. High Perform. Comput. Appl.* **14**(1), 65–81 (2000)
- Guan, K.M., Nazarova, M., Guo, B., Tchelepi, H., Kovscek, A.R., Creux, P.: Effects of image resolution on sandstone porosity and permeability as obtained from x-ray microscopy. *Transp. Porous Media.* 1–13 (2018)
- Guibert, R., Horgue, P., Debenest, G., Quintard, M.: A comparison of various methods for the numerical evaluation of porous media permeability tensors from pore-scale geometry. *Math. Geosci.* **48**(3), 329–347 (2016)
- Guibert, R., Nazarova, M., Horgue, P., Hamon, G., Creux, P., Debenest, G.: Computational permeability determination from pore-scale imaging: sample size, mesh and method sensitivities. *Transp. Porous Media* **107**(3), 641–656 (2015)
- Guo, B., Ma, L., Tchelepi, H.A.: Image-based micro-continuum model for gas flow in organic-rich shale rock. *Adv. Water Resour.* **122**, 70–84 (2018)
- Horgue, P., Guibert, R., Gross, H., Creux, P., Debenest, G.: Efficiency of a two-step upscaling method for permeability evaluation at Darcy and pore scales. *Comput. Geosci.* **19**(6), 1159–1169 (2015)
- Janert, P.: Data analysis with open source tools: a hands-on guide for programmers and data scientists. “O'Reilly Media Inc” (2010)
- Jiang, Z., Wu, K., Couples, G., van Dijke, M., Sorbie, K., Ma, J.: Efficient extraction of networks from three-dimensional porous media. *Water Resour. Res.* **43**(12) (2007)
- Landauer, R.: The electrical resistance of binary metallic mixtures. *J. Appl. Phys.* **23**(7), 779–784 (1952)
- Liang, Z., Ioannidis, M., Chatzis, I.: Geometric and topological analysis of three-dimensional porous media: pore space partitioning based on morphological skeletonization. *J. Colloid Interface Sci.* **221**(1), 13–24 (2000)

30. Lindquist, W., Venkatarangan, A.: Investigating 3D geometry of porous media from high resolution images. *Phys. Chem. Earth Part A: Solid Earth Geodesy* **24**(7), 593–599 (1999)
31. Lindquist, W.B., Lee, S.M., Coker, D.A., Jones, K.W., Spanne, P.: Medial axis analysis of void structure in three-dimensional tomographic images of porous media. *Journal of Geophysical Research: Solid Earth* **101**(B4), 8297–8310 (1996)
32. Lotufo, R.A., Zampiroli, F.A.: Fast multidimensional parallel euclidean distance transform based on mathematical morphology. In: *Proceedings XIV Brazilian Symposium on Computer Graphics and Image Processing*, pp. 100–105. IEEE (2001)
33. Martin, H.: Lubrication of gear teeth. *Engineering* **102**, 119 (1916)
34. Meijster, A., Roerdink, J.B., Hesselink, W.H.: A General Algorithm for Computing Distance Transforms in Linear Time. In: *Mathematical Morphology and Its Applications to Image and Signal Processing*, pp. 331–340. Springer (2002)
35. Mourzenko, V., Thovert, J.F., Adler, P.: Conductivity and transmissivity of a single fracture. *Transp. Porous Media* **123**(2), 235–256 (2018)
36. Muljadi, B.P., Blunt, M.J., Raeini, A.Q., Bijeljic, B.: The impact of porous media heterogeneity on non-Darcy flow behaviour from pore-scale simulation. *Adv. Water Resour.* **95**, 329–340 (2016)
37. Palágyi, K., Balogh, E., Kuba, A., Halmi, C., Erdöhelyi, B., Sorantin, E., Hausegger, K.: A Sequential 3D Thinning Algorithm and Its Medical Applications. In: *Biennial International Conference on Information Processing in Medical Imaging*, pp. 409–415. Springer (2001)
38. Plouraboué, F., Flukiger, F., Prat, M., Crispel, P.: Geodesic network method for flows between two rough surfaces in contact. *Phys. Rev. E* **73**(3), 036305 (2006)
39. Plouraboué, F., Geoffroy, S., Prat, M.: Conductances between confined rough walls. *Phys. Fluids* **16**(3), 615–624 (2004)
40. Pudney, C.: Distance-ordered homotopic thinning: a skeletonization algorithm for 3D digital images. *Comput. Vis. Image Understand.* **72**, 404–413 (1998)
41. Raeini, A.Q., Bijeljic, B., Blunt, M.J.: Generalized network modeling: network extraction as a coarse-scale discretization of the void space of porous media. *Phys. Rev. E* **96**(1), 013312 (2017)
42. Raeini, A.Q., Blunt, M.J., Bijeljic, B.: Modelling two-phase flow in porous media at the pore scale using the volume-of-fluid method. *J. Comput. Phys.* **231**(17), 5653–5668 (2012)
43. Saha, P.K., Borgfors, G., di Baja, G.S.: A survey on skeletonization algorithms and their applications. *Pattern Recogn. Lett.* **76**, 3–12 (2016)
44. Saxena, N., Hofmann, R., Alpak, F.O., Berg, S., Dieterich, J., Agarwal, U., Tandon, K., Hunter, S., Freeman, J., Wilson, O.B.: References and benchmarks for pore-scale flow simulated using micro-CT images of porous media and digital rocks. *Adv. Water Resour.* **109**, 211–235 (2017)
45. Saxena, N., Hows, A., Hofmann, R., Alpak, F.O., Freeman, J., Hunter, S., Appel, M.: Imaging and computational considerations for image computed permeability: operating envelope of digital rock physics. *Adv. Water Resour.* **116**, 127–144 (2018)
46. Sheppard, A., Sok, R., Averdunk, H., Robins, V., Ghous, A.: Analysis of rock microstructure using high-resolution x-ray tomography. In: *Proceedings of the International Symposium of the Society of Core Analysts*, pp. 1–12 (2006)
47. Sherbrooke, E.C., Patrikalakis, N.M., Brisson, E.: An algorithm for the medial axis transform of 3D polyhedral solids. *IEEE Trans. Vis. Comput. Graph.* **2**(1), 44–61 (1996)
48. Siddiqi, K., Bouix, S., Tannenbaum, A., Zucker, S.W.: Hamilton-Jacobi skeletons. *Int. J. Comput. Vis.* **48**(3), 215–231 (2002)
49. Silverstein, C.: Google performance tools (2011)
50. Spanne, P., Thovert, J., Jacquin, C., Lindquist, W., Jones, K., Adler, P.: Synchrotron computed microtomography of porous media: topology and transports. *Phys. Rev. Lett.* **73**(14), 2001 (1994)
51. Stroud, D.: Generalized effective-medium approach to the conductivity of an inhomogeneous material. *Phys. Rev. B* **12**(8), 3368 (1975)
52. Stroud, D.: The effective medium approximations: some recent developments. *Superlattices Microstruct.* **23**(3-4), 567–573 (1998)
53. Sudakov, O., Burnaev, E., Koroteev, D.: Driving digital rock towards machine learning: predicting permeability with gradient boosting and deep neural networks. *Comput. Geosci.* **127**, 91–98 (2019)
54. Torquato, S.: *Random heterogeneous materials: microstructure and macroscopic properties*, vol. 16. Springer Science & Business Media (2013)
55. Torsello, A., Hancock, E.R.: Correcting curvature-density effects in the Hamilton–Jacobi skeleton. *IEEE Trans. Image Process.* **15**(4), 877–891 (2006)
56. Tschumperlé, D.: The CImg Library. In: *IPOL 2012 Meeting on Image Processing Libraries*, pp. 4–Pp (2012)
57. Weller, H.G., Tabor, G., Jasak, H., Fureby, C.: A tensorial approach to computational continuum mechanics using object-oriented techniques. *Comput. Phys.* **12**(6), 620–631 (1998)
58. Wildenschild, D., Sheppard, A.P.: X-ray imaging and analysis techniques for quantifying pore-scale structure and processes in subsurface porous medium systems. *Adv. Water Resour.* **51**, 217–246 (2013)
59. Zhao, H.Q., Macdonald, I.F., Kwiecien, M.J.: Multi-orientation scanning: a necessity in the identification of pore necks in porous media by 3-D computer reconstruction from serial section data. *J. Colloid Interface Sci.* **162**(2), 390–401 (1994)